X-ray standing wave induced Compton and elastic scattering from thin periodic multilayer structures

M. K. Tiwari,[1,*] H. Wang,[2] K. J. S. Sawhney,[2] M. Nayak,[1] and G. S. Lodha[1]

[1]*Indus Synchrotrons Utilization Division, Raja Ramanna Centre for Advanced Technology, Indore-452013 (M P), India*

[2]*Diamond Light Source Ltd, Harwell Science and Innovation Campus, Didcot, Oxfordshire OX11 0DE, United Kingdom*

(Received 1 February 2013; published 3 June 2013)

We report determination of structural parameters on angstrom length scale of nanostructured periodic multilayers using x-ray standing wave (XSW) enhanced elastic and Compton scattering. We show that the elastic scattered x-ray intensities emitted from the thin periodic multilayer structures, under strong XSW condition, are largely sensitive to the structural parameters of high-z layers, whereas the Compton scattered intensities are sensitive to the parameters of low-z layers. The utility of the methodology is demonstrated by analyzing two repetitive W/B_4C multilayer structures with different surface-interface properties. The results are compared with those obtained using x-ray reflectivity and conventional x-ray standing wave fluorescence techniques. It is further shown that the Bragg angle can be derived with high accuracy ($\sim 0.002^\circ$) from the ratio of the scattering intensities, which in turn improves the accuracy of the derived multilayer periodicity. The method presents an opportunity to probe structures on angstrom length scale of any periodic multilayer structure comprising of low atomic number layers. Unlike the conventional XSW fluorescence measurements, the present method has an advantage that it permits the determination of structural parameters of both the high- and the low-z layers independently.

DOI: 10.1103/PhysRevB.87.235401 PACS number(s): 68.49.Uv, 78.70.Ck, 78.67.Pt, 07.85.Qe

I. INTRODUCTION

Periodic synthetic multilayer structures consisting of alternating thin layers of the high- and low-z elements or compounds[1,2] offer unique structural,[3] magnetic,[4,5] and electronic[6,7] properties with a wide range of applications. Multilayers as an x-ray optical element are used in many technological applications like x-ray astronomy, microscopy, and spectroscopy. They are also employed as filters and monochromators in synchrotron radiation and free-electron x-ray lasers. The performance of a multilayer structure strongly depends on its microstructural properties such as thickness of individual high- and low-z layers, interface roughness, and interlayer formation, etc. These microstructural parameters are usually determined from the x-ray reflectivity[8] (XRR), x-ray scattering,[9,10] or the x-ray standing wave (XSW) induced fluorescence and photoelectrons emission (PEE) measurements.[11–16] The PEE technique offers analysis for both the high- and low-z constituents, however it is basically a surface sensitive technique. The XRR technique is a reliable method to measure structural parameters such as thickness and interface roughness at subnanometer length scale, as demonstrated for metallic, intermetallic, semiconducting, and ceramic thin film mediums. The conventional XRR technique, however, has the limitation that it does not provide any element-specific information. It only provides the composite thickness and roughness values for the high- and low-z layer mediums, and sometimes it becomes quite difficult to establish the true microstructural parameters of the periodic multilayers.

Fluorescence-assisted XSW technique as a structural probe has the potential of being one of the most powerful and versatile tools for characterization of thin periodic multilayers, as it combines the features of both x-ray reflectivity and x-ray fluorescence techniques. The method has been widely used for large numbers of applications; determination of positions of impurity atoms in crystals,[17–19] dispersion of absorbed atoms[20–23] and metal nanoparticles on surfaces,[24,25] and to study interface structure and density variations in multilayers.[26,27] Usually, an XSW induced fluorescence signal emitted from periodic multilayers offers direct determination of structural properties of the high-z layers. This is because the fluorescence signal from the low-z layer is often weak due to its low fluorescence yield as well as the strong self absorption in the layered medium. Thus, structural information of the low-z layers is obtained indirectly from the XSW fluorescence measurements of the high-z layers. Scattered x-ray intensities (elastic and Compton) emitted from a multilayer under strong Bragg reflection condition also contain the information about structural parameters of the thin film medium. In practice, however, it is very difficult to retrieve such information. To the best of our knowledge, attempt has not been made previously to exploit XSW enhanced elastic and Compton scattered x rays for determination of structural properties of the low-z containing periodic multilayer structures. The understanding of the XSW induced glancing incidence angle dependent Compton and elastic profiles is nontrivial for its potential utility in case of study of real thin film systems and hence needs to be addressed properly. For many applications determination of structural properties of the individual layers is important, for example, in x-ray wave guide structures (trilayers) where a thick low-z layer is sandwiched between two high-z layers. In such a multilayer structure x-ray compression efficiencies are closely related to the surface-interface properties of the high- and low-z layers. Only a few research groups[28,29] have reported XSW enhanced x-ray elastic scattering measurements from the periodic multilayer structures with an aim to determine amorphous-crystalline properties and diffuse scattered intensities originated from the interface of the two-layer media.

In the present work, we address how XSW enhanced Compton and elastic x rays can be used to determine microstructural properties of the thin periodic multilayer structures. Here, we

1098-0121/2013/87(23)/235401(11) ©2013 American Physical Society

provide a detailed mathematical description for computation of glancing incidence angle dependent Compton and elastic scattering profiles in case of rough and intermixed periodic multilayer structures. We have applied the new approach for the determination of microstructural properties of two different W/B_4C repetitive multilayer structures using synchrotron x rays. Our method works on the general assumption that the XSW enhanced elastic x-ray scattering profile from a multilayer medium is largely sensitive to the x-ray scattering cross section of the high-z layers, whereas the Compton scattering profile is sensitive to the x-ray scattering cross section of the low-z layers. We correlate this property to structural parameters of the high- and low-z layers with their measured XSW enhanced elastic and Compton scattering profiles. Unlike the conventional XSW fluorescence approach, the method self-consistently allows the determination of information on both high- and low-z layers *independently*. In contrast to the established PEE technique, which has specific probing depths of approximately from ∼1–10 nm for partial to total electron yield, the present approach provides spatially depth-resolved sensitivities with angstrom level resolution through structures up to several hundreds of nanometer thickness ranging from free surface to deeply embedded layers in a nondestructive manner. Furthermore, the present methodology permits measurements of several XSW profiles (elastic, Compton, and fluorescence) simultaneously. Fitting these profiles in a feedback sequence to each other helps to minimize the uncertainties of fitted results for the combined dataset which ensure the real physical values.

II. THEORETICAL BACKGROUND

A. Calculation of the Compton and elastic scattering from the periodic multilayer structures

The electromagnetic x-ray field intensity distribution inside a thin layer medium can be calculated by applying recursive[11,12] and matrix methods.[13] For simplicity we assume a multilayer structure consisting of N stacks deposited on a thick flat substrate as shown in Fig. 1. The transmitted (E_j^t) and reflected (E_j^r) electric field amplitudes of a plane electromagnetic wave $E_j(r) = E_j \exp[i(\omega \times t - k_j \times r)]$ traveling with frequency ω at the top of jth layer can be calculated using recursive approach.[11] The normalized x-ray field intensity I_j $(\theta,\ Z)$ in the jth layer medium of a multilayer structure, at depth Z, (measured from the interface above) is given by

$$I_j(\theta,Z) = \frac{|E_j^t + E_j^r|^2}{|E_j^t|^2} = \left\{ \exp(-2k''_{j,z}Z) + \left|\frac{E_j^r}{E_j^t}\right|^2 \exp(2k''_{j,z}Z) + 2\left|\frac{E_j^r}{E_j^t}\right| \cos[\nu(\theta) + 2k'_{j,z} \times Z] \right\}, \quad (1)$$

where $k'_{j,z}$ and $k''_{j,z}$ represent the real and imaginary part of the z component of wave vector k. The components of wave vector k in the jth layer can be written as

$$k_{j,x} = \frac{2\pi}{\lambda}\cos\theta,\ k_{j,z} = \frac{2\pi}{\lambda}(\varepsilon_j - \cos^2\theta)^{1/2},$$

where $\varepsilon_j = 1 - 2\delta_j - i2\beta_j$ is the complex dielectric constant of medium j, λ is the wavelength of incident radiation, and δ_j and β_j are the optical constants of the jth medium.

The scattered x-ray intensities (elastic and Compton), emitted from the jth layer of a multilayer structure can be evaluated by

$$I_j^{\text{elastic}}(\theta) \propto \sigma_{\text{elastic}}(E_0) \times \int_0^d I_j(\theta,Z) \times \exp\left[-\left(\frac{(\mu/\rho)_{E_0}}{\sin\phi}\right)\rho \times Z\right] dZ, \quad (2)$$

$$I_j^{\text{Compton}}(\theta) \propto \sigma_{\text{Compton}}(E_0) \times \int_0^d I_j(\theta,Z) \times \exp\left[-\left(\frac{(\mu/\rho)_{E}}{\sin\phi}\right)\rho \times Z\right] dZ, \quad (3)$$

where d is the thickness of the jth layer and ρ is the density of the layer j in g/cm^3. σ_{elastic}, σ_{Compton} are the elastic and Compton x-ray cross sections of the jth layer element at incident x-ray energy of E_0. These x-ray cross sections largely depend on the atomic number (z) of the material (i.e., $\sigma_{\text{elastic}} \propto$-$z^2$, and $\sigma_{\text{Compton}} \propto$-$z$) as described in the Appendix and their values can be evaluated from the McMaster[30] and Hubbell tables.[31] Also, many software packages[32–34] are available, which can be used to compute x-ray cross sections of different materials at given x-ray energies. $(\mu/\rho)_{E_0}$ and $(\mu/\rho)_E$ respectively represent mass attenuation coefficients (in cm^2/g) for the layer j at excitation energy E_0, and at the mean Compton scattered x-ray energy of E. φ is the takeoff angle for the emitted scattered x rays measured with respect to multilayer surface ($\varphi \sim 90^\circ$ in our case). The total elastic or Compton scattered x-ray intensity emitted from a multilayer structure can be obtained by summing the contribution from all layers including the Si substrate and taking into account the absorption correction of upper layers.[35] A part of the scattered x rays originating from the infinitely thick substrate (Si substrate) adds a fixed background to the elastic and the Compton scattering profiles. The substrate contribution does not produce any influence on the structural information of

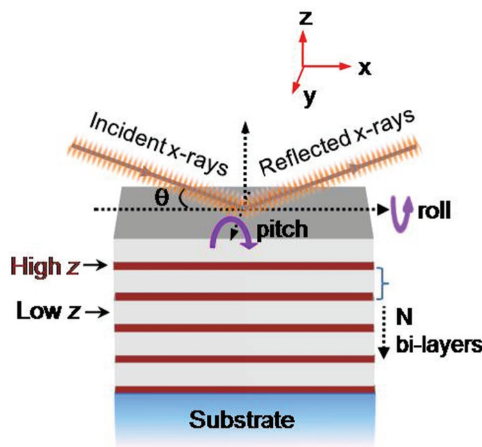

FIG. 1. (Color online) A schematic representation for x-ray reflection from a periodic multilayer structure.

multilayer structure, derived from the measured elastic or Compton scattering profiles.

B. Examples of calculations

To investigate the validity of the XSW enhanced elastic and Compton scattering method for microstructural characterization of periodic multilayer structures, we have performed numerical simulations. Figure 2(a) depicts the calculated x-ray field intensity distribution [Eq. (1)] inside an ideal (interfacial roughness $\sigma = 0.0$ nm) W/B_4C periodic multilayer structure ($d = 4.0$ nm, structure factor $\Gamma = 0.437$, number of bilayers $N = 10$) as a function of incidence angle and multilayer depth (Z), while Fig. 2(b) presents angle-dependent variation of the Compton and elastic scattered intensity profiles in the vicinity of the first-order Bragg peak. For these calculations, incident x rays of energy 15 keV are assumed. From Fig. 2(a), it can be seen that below the critical angle ($\theta_c \sim 0.216°$), x-ray intensity does not penetrate into the multilayer medium and rather it exists on top of the multilayer surface in the form of XSW field. As the incidence angle crosses the critical angle boundary, the x-ray fields start to penetrate the layers of the multilayer medium. At the Bragg angle, an XSW field of periodicity equal to the multilayer period is set up inside the multilayer structure. This XSW field also extends above the multilayer surface. Figure 2(b) shows the net elastic and Compton scattered x-ray intensities [Eqs. (2) and (3)] emitted from the multilayer structure as a function of incidence angle over the Bragg peak region. It can be seen that the two profiles are distinctly different from each other and vary in a peculiar way across the Bragg region. These profiles also exhibit the Kiessig fringes similar to what are observed in x-ray reflectivity profiles, arising from the total stack thickness of the multilayer structure. The elastic scattering yield increases at the high angle side of the Bragg peak because in this condition the XSW antinodes coincide with the position of the W layers in the multilayer medium and as a result one observes an increased elastic scattering yield from the W layers. Conversely, the Compton scattering yield increases at the low angle side of the Bragg peak because in this condition the XSW antinodes coincide with the position of the B_4C layers in the multilayer medium and as a result the Compton scattering cross section increases from the low-z layers. The simulated spectra show that the angle-dependent profiles of different scattered photons (elastic, Compton, and fluorescent x rays) emitted from thin layered materials, are primarily sensitive to the atomic numbers of the constituent layers (high-z and low-z layers). The elastically scattered x rays essentially originate from the high-z layers while the Compton contribution mostly arises from the low-z layers. Because, at a given x-ray energy, the elastic x-ray cross section ($\sigma_{\text{elastic}} \propto$-$z^2$) and the Compton x-ray cross section ($\sigma_{\text{Compton}} \propto$-$z$) strongly depend on the atomic number of a material, thus, XSW enhanced measurements of the Compton and elastic x-ray scattering intensities from a thin periodic multilayer medium enable determination of structural properties of both the high- and low-z layers separately.

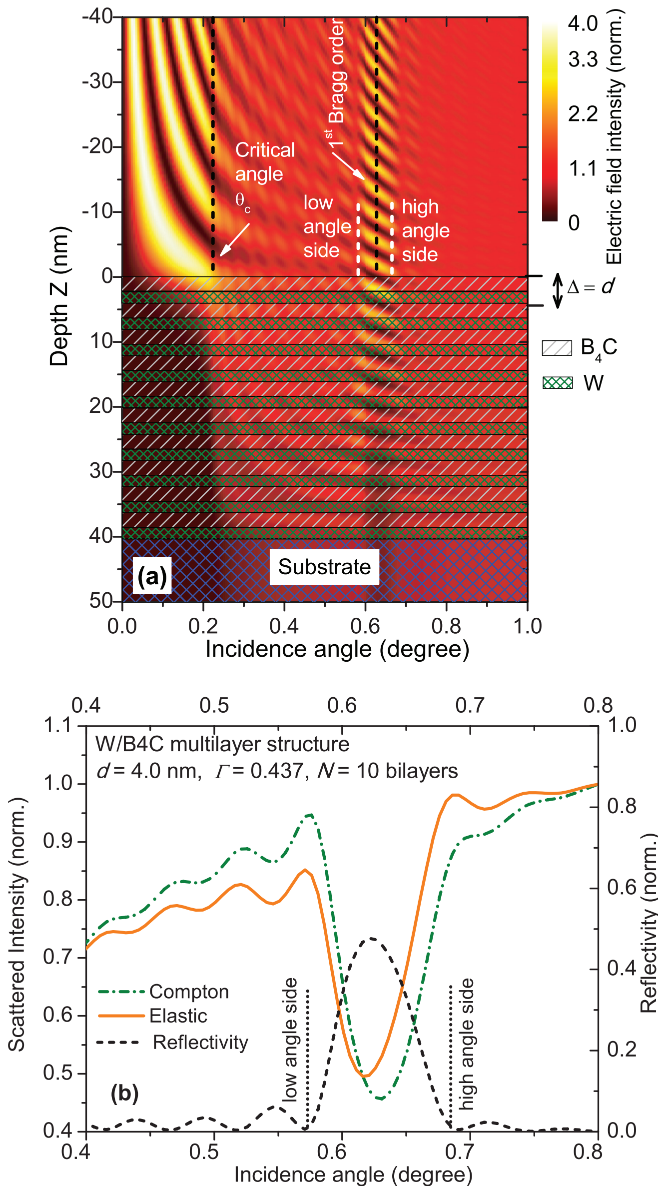

FIG. 2. (Color online) (a) Calculated x-ray field intensity distribution inside an ideal W/B_4C periodic multilayer structure ($d = 4.0$ nm, structure factor $\Gamma = 0.437$, number of bilayers $N = 10$) as a function of incidence angle and film depth (Z). Here, multilayer structure factor Γ, is described as the ratio of the low-z layer thickness to total bilayer period thickness d. (b) Calculated grazing incidence angle-dependent profiles for the Compton and elastic scattered x rays in the vicinity of the first-order Bragg peak. Incident x rays of energy 15.0 keV were used as excitation energy in these calculations. The calculated XRR profile of the multilayer structure across the Bragg region is also plotted.

Usually, the position of the Bragg angle for a periodic multilayer structure is determined using the XRR technique. The maximum point of the Bragg peak reflectivity curve delineates the correct position of the Bragg angle. However, the maximum point in the Bragg peak occurs in a nearly flat region within the angular range of ~0.1 milliradian, which limits accuracy for its determination. Shaw *et al.*[36] have described in detail the calculation procedures for the Bragg angle for synthetic multilayer x-ray reflectors. Here we demonstrate how the XSW assisted Compton and elastic scattering measurements can be utilized for an accurate determination of the Bragg angle position, which in turn facilitates precise determination of the

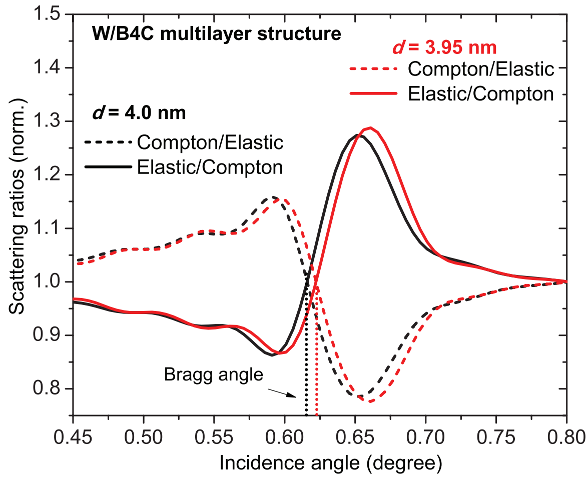

FIG. 3. (Color online) Calculated elastic and Compton scattering ratio profiles in the vicinity of first-order Bragg peak for the two different periodic multilayer structures at incident x-ray energy 15.0 keV. In calculations, the bilayer period d of the multilayers has been varied with small value ∼0.05 nm in order to demonstrate the thickness sensitivity of the scattering ratios. The point of intersection of the scattering ratio profiles provides the value of the Bragg angle (represented by vertical dotted lines).

multilayer d periodicity. We have plotted scattering ratios (Compton-to-elastic and elastic-to-Compton) as a function of incidence angle for two representative W/B_4C multilayer structures having small variation in their d-period thickness of ∼0.05 nm as shown in Fig. 3. In calculations we have assumed ten bilayers for each multilayer structure. Here, it can be seen that the angle-dependent scattering ratio profiles generate a XSW-like envelope in the vicinity of the Bragg peak region. This XSW envelope shifts to low or high angle sides if there is a small variation in the multilayer periodicity. The point of intersection of two scattering ratio profiles defines position of the Bragg angle for a multilayer structure. Since the intersection point lies on the slope of the scattering ratio profiles, it provides precise determination of the Bragg angle value with improved accuracies of ∼0.002°.

III. CASE STUDIES

A. Effect of variation of layer thickness and interface roughness

In this section we present results of calculations, which demonstrate how the XSW enhanced Compton and elastic profiles can be used as a sensitive probe to determine the microstructural properties such as thickness and roughness of any periodic multilayer structure. We consider a periodic multilayer structure consisting of $N = 10$ bilayers of W/B_4C materials on top of a Si substrate and we have calculated grazing incidence angle-dependent Compton and elastic scattering profiles for different thickness and roughness values of the individual high- and low-z layers. As stated earlier, the major contribution to the Compton scattering occurs from the low-z layers while the elastic scattering is dominated by the high-z layers, therefore we have evaluated the two scattering profiles individually. In Fig. 4(a), we show the simulated Compton scattering profiles for different thickness of the B_4C layers. The thickness of B_4C layers is changed in the range of 2.2–2.3 nm

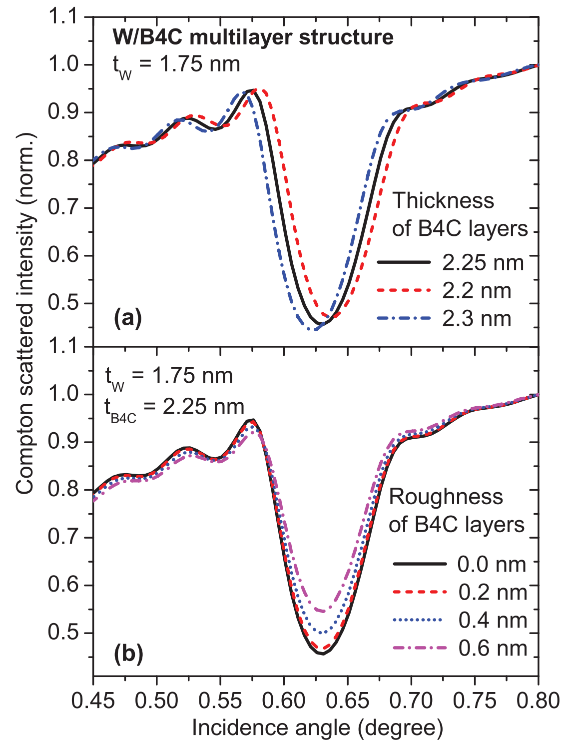

FIG. 4. (Color online) The Compton scattering profiles calculated for a W/B_4C periodic multilayer structure having ten bilayers on a Si substrate. The simulations have been performed by changing different microstructural parameters of B_4C layers. (a) Effect of thickness of B_4C layers has been examined. (b) Effect of roughness of B_4C layers has been evaluated. From these figures it can be seen that angle-dependent Compton scattering profile across the Bragg region is fairly sensitive to the microstructural parameters of the low-z layers.

while the thickness of the W layers is kept at a constant value of $t_W = 1.75$ nm.

It can be seen from Fig. 4(a) that the Compton scattering profile shows a distinct and systematic variation as we allow the B_4C layer thickness to gradually vary. Next, we have studied the effect of the interface roughness of the B_4C layers on the Compton scattering profiles. The Compton scattering profiles have been simulated assuming different interface roughness values in the range $\sigma_{B4C} = 0.0$ to 0.6 nm. For these calculations, we consider an ideal interface for the W layers, i.e., $\sigma_W = 0$ nm. The simulation results are shown in Fig. 4(b), from which it can be seen that the Compton scattering profile shows a systematic variation as the interface roughness of the B_4C layers is progressively increased. The contrast of the XSW induced Compton scattering profile across the Bragg region decreases at high interface roughness of the B_4C layers due to the drop in the Bragg peak reflectivity.

In a similar way, the elastic scattering profile has also been examined for the variation of microstructural properties of the W layers. In Fig. 5(a), the simulated elastic scattering curves for different thickness values of W layers are plotted. The thickness of the W layers is varied in steps of 0.05 nm in the range of 1.7–1.8 nm, while the thickness of the B_4C layers is set to $t_{B4C} = 2.25$ nm. It can be observed that the angle-dependent elastic scattering intensity profile changes in a similar way to that described in Fig. 4(a). This is mainly attributed to the

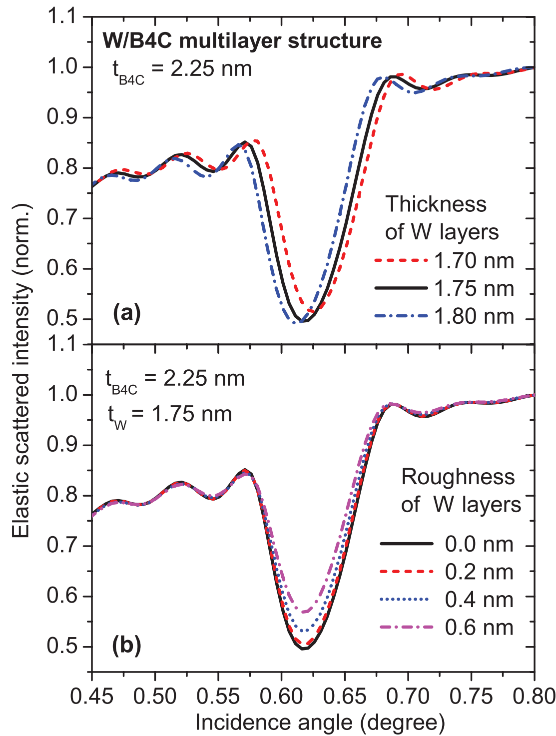

FIG. 5. (Color online) Calculated elastic scattering profiles for a W/B_4C periodic multilayer structure comprised of ten bilayers on a Si substrate. The effect of variation of thickness (a), and roughness (b) of the W layers has been examined. It is observed that the angle-dependent elastic scattering profile across the Bragg region is fairly sensitive to the microstructural parameters of the high-z layers.

change in average d-period value of the multilayer structure. Figure 5(b) illustrates the effect of interface roughness of the W layers on the XSW enhanced elastic scattering profile. It is evident from this figure that the elastic scattering profile changes significantly as the roughness of the W layers σ_W is varied. As an example, we have varied the roughness of the W layers in the range of 0.0 to 0.6 nm.

The above simulation results clearly demonstrate that the XSW enhanced Compton and elastic scattering profiles are fairly sensitive to the microstructural properties of periodic multilayer structures, similar to conventional x-ray reflectivity and fluorescence-assisted XSW profiles.

B. Interface mixing

In this section, the interface mixing effects in periodic multilayer structures have been addressed by assuming the presence of an additional interlayer medium at the interface boundary of the high- and low-z layers. A schematic presentation of the formation of an interface layer between the high- and low-z layer mediums is pictorially shown in the inset of Fig. 6(a). As we have discussed in Sec. II B, the elastically scattered intensity from a multilayer largely emanates from the high-z layers. Figure 6(a) demonstrates simulation results for the elastic scattering profile for the thickness variations of the intermixed layer. Here, the thickness of the intermixed layer has been varied from 0.0 to 1.0 nm keeping the average d-period thickness of the multilayer structure to a fixed value of ~4.0 nm. This is achieved by assuming the formula $d = t_{\text{interlayer}} + (t_w - \frac{t_{\text{interlayer}}}{2}) + (t_{\text{B4C}} - \frac{t_{\text{interlayer}}}{2})$ where t_w describes the thickness of the W layers, t_{B4C} represents the thickness of the B_4C layers and $t_{\text{interlayer}}$ is the thickness of the intermixed layer. In all the calculations, the thickness of the interlayer medium is assumed to be ~1.0 nm. It can be seen that the elastic scattering profile in the Bragg angle region changes dramatically as thickness of interface layer is varied. It can be further seen that the shape of the elastic scattering profile changes more rapidly at the high angle side of the Bragg peak compared to the low angle side. The peak to valley contrast of the XSW oscillation in the vicinity of the Bragg peak decreases

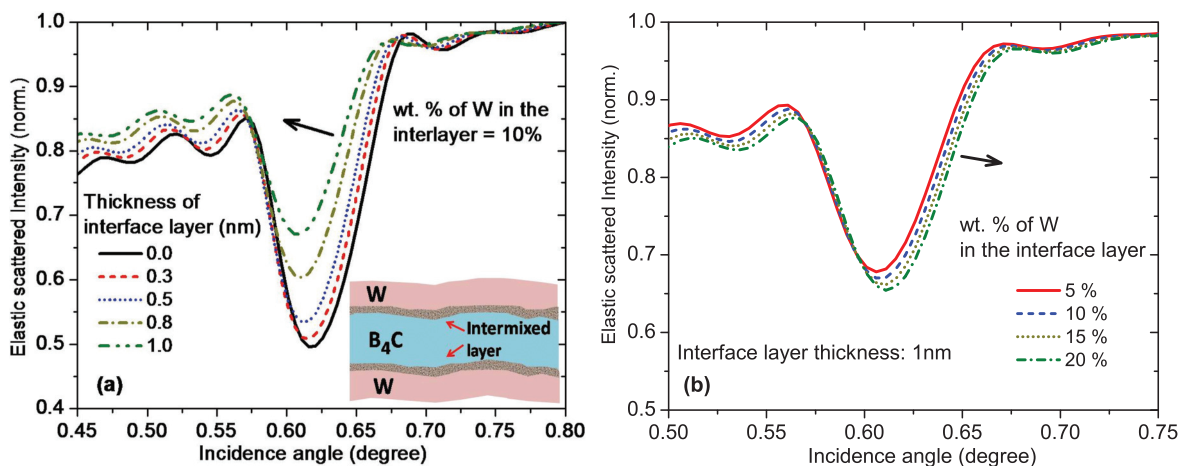

FIG. 6. (Color online) Calculated plots for the elastic scattering profiles for a W/B_4C periodic multilayer ($d \approx 4.0$ nm, structure factor $\Gamma \sim 0.437$) for the case when intermixing occurs between the high- and low-z layers at the interface boundary. (a) Effect of variation of interlayer thickness is evaluated assuming a composition of interlayer W ≈ 10 at.% and B_4C ≈ 90 at.%. The inset shows a schematic illustration for interlayer formation at the boundary of W and B_4C layers. (b) Demonstrates effect of composition variation of W element in the interlayer. The thickness of intermixed layer was kept constant at ~1 nm. It is observed that the angle-dependent elastic scattering profile across the Bragg region is fairly sensitive to the structural properties of the intermixed layer. All these calculations were done considering ten bilayers of the W/B_4C multilayer on a Si substrate.

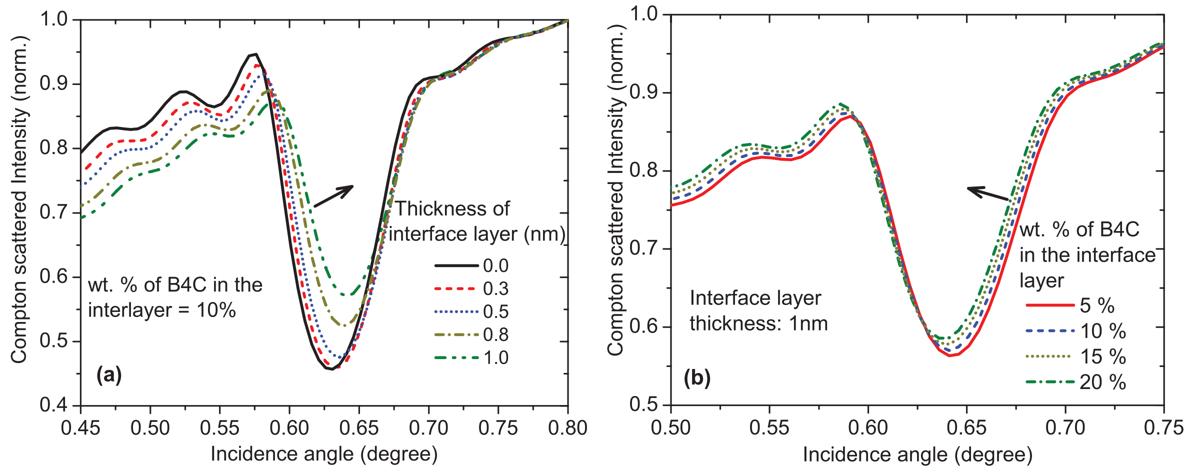

FIG. 7. (Color online) Calculated plots for the Compton scattering profiles for a W/B_4C multilayer structure ($d \approx 4.0$ nm, structure factor $\Gamma \sim 0.437$). (a) Effect of variation of interlayer thickness, assuming the composition of the interlayer to be W ≈ 90 at.% and $B_4C \approx 10$ at.%. (b) Effect of composition variation of B_4C in the interlayer. All these calculations are done considering ten bilayers of W/B_4C multilayer on a Si substrate with thickness of interlayer kept constant at ∼1 nm.

as the thickness of the interface layer is increased. This arises due to a drop in the density contrast among the high- and low-z layers in the periodic multilayer structure. Since the interlayer medium is assumed to be rich in B_4C concentration (at.% of W = 10% and at.% of B_4C = 90%), the XSW induced elastic scattering profile shifts toward the low angle side as we increase the thickness of the interlayer. In Fig. 6(b), the simulation results for the elastic profile have been presented for the change of at. concentrations of W element. As the concentration of W in the interlayer medium increases, its density also increases. As a result, the XSW oscillation in the elastic profile shifts towards the higher angle side of the Bragg peak. From these simulation results, it is clear that the XSW induced elastic scattering profile is also sensitive to the density variation of the high-z layers.

Next, we demonstrate by simulations how the XSW induced Compton scattering profile is susceptible to the small density variations of the low-z medium in periodic multilayers. Assuming now that the interlayer medium is mainly composed of W atoms (at.% of W ≈ 90% and at.% of $B_4C \approx 10\%$), the Compton scattering profiles have been calculated for different thicknesses of the interlayer medium. It can be seen from Fig. 7(a) that as the thickness of the interlayer medium is increased from 0 to 1.0 nm, the XSW oscillation in the Compton scattering profile moves towards the high angle side of the Bragg peak, conversely to the case of the elastic scattering profile [Fig. 6(a)]. The sensitivity of the Compton scattering profile to the variation of at. concentration of B_4C in the intermixed layer is presented in Fig. 7(b). Here, it can be observed that as the at.% of B_4C compound in the intermixed medium increases the Compton scattering profile shifts towards the low angle side of the Bragg peak. This occurs due to the drop in the average density of the intermixed medium, as we increase the at.% of B_4C. In these calculations, the thickness of the intermixed medium is kept constant at ∼1.0 nm. It can be seen that the Compton scattering profile changes significantly even with a few atomic percentage change of B_4C atoms in the intermixed medium. These simulation results clearly show that the Compton and elastic scattering profiles provide the information on both the low- and high-z layers independently even when significant interface mixing occurs. Thus, the XSW induced scattering measurements offer an opportunity for a possibility to characterize microstructural parameters of the high- and low-z layer individually.

IV. EXPERIMENT

Various W/B_4C multilayer structures comprising of a nominal bilayer period $d \sim 40$ Å were fabricated on the polished Si (100) substrates at room temperature using a magnetron sputtering system. Before deposition, the r.m.s. roughness of the Si substrates was determined using a laboratory source x-ray reflectometer and was found to be ∼5 ± 1 Å. Argon was employed as the sputtering gas medium. During deposition, the vacuum in the chamber was maintained in the range of $\sim 5 \times 10^{-3}$ mbar whereas the base vacuum was $\sim 2 \times 10^{-8}$ mbar before start off the deposition process. The deposition rate was kept constant at ∼5 Å/min. The details of the deposition system are given elsewhere.[37]

Grazing incidence angle-dependent Compton and elastic x-ray scattering measurements of the multilayer structures were carried out on the B16 Test beamline of the Diamond Light Source, UK.[38] For the measurements reported here, we used collimated x rays of energy 15 keV, monochromatized using a Si (111) double crystal monochromator. Incident x-ray beam of size ∼50 μm (v) × 5 mm (h) was allowed to excite W/B_4C multilayer structures, at grazing incidence angles. The XSW and XRR measurements on the multilayer samples were performed using a five-axis Huber diffractometer in θ–2θ geometry, in the ambient air environment. The measurements were carried out in the top-up operation mode of Diamond, at a ring current of 250 mA. The multilayer samples were mounted on the sample stage of the diffractometer, which consists of three (XYZ) precision motorized stages. These stages facilitate the alignment of the multilayer samples with accuracies better than 1 μm. We also employed an optical

microscope for preliminary visual alignment of the samples; however, the final alignment was done using x rays. The measured sphere of confusion (SOC) of the diffractometer station over the full range of all five axes, with a sample load of 20 kg, was better than 60 μm. Fluorescent and scattered x-ray intensities emitted from the multilayer samples were dispersed and collected by a Vortex energy dispersive spectroscopy detector, placed vertically normal to the sample surface. A 2-mm Al collimator was used between the sample and detector to maintain a constant solid angle of detection on the sample surface, at various incidence angles. The fluorescence measurements were performed for an acquisition live time of 40 s at each angular position of the sample. To measure the specular reflected x-ray intensities from the sample, an avalanche photodiode detector (APD), capable of measuring very high count rates and having a large dynamic range, was employed.

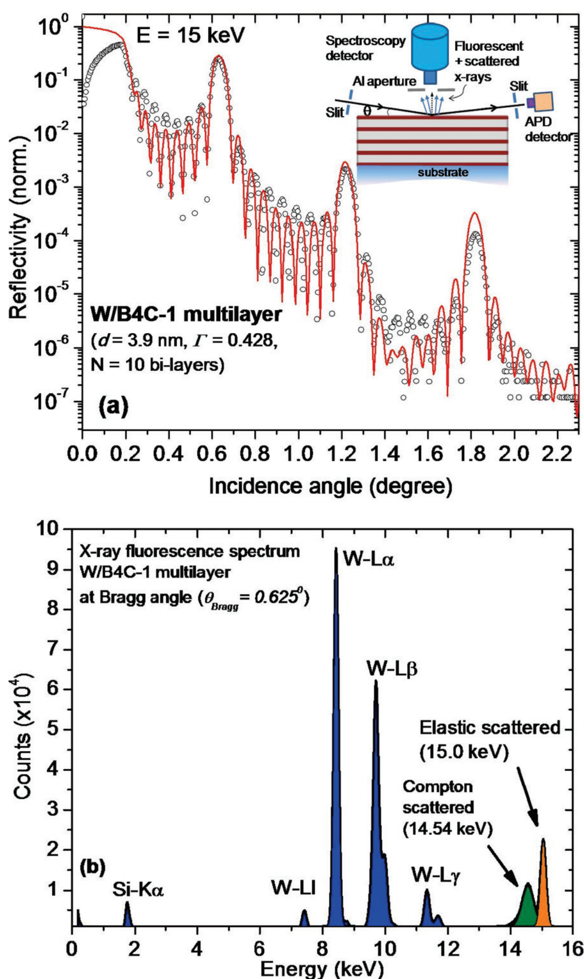

FIG. 8. (Color online) (a) Measured and fitted XRR profiles for a W/B_4C-1 multilayer ($d \approx 3.9$ nm, structure factor $\Gamma \sim 0.428$) at 15 keV x-ray energy. (b) Shows energy dispersive x-ray fluorescence spectrum of multilayer structure, measured at the Bragg angle ($\theta = 0.625^\circ$). The inset of Fig. 8(a) shows geometry of the experimental setup used for the XRR and XSW enhanced Compton and elastic scattering measurements.

V. RESULTS AND DISCUSSION

Figure 8(a) shows the XRR pattern of a W/B_4C multilayer structure on a Si substrate measured at 15 keV x-ray energy. The inset in the figure provides the geometry of the experimental setup. The measured XRR data was fitted with the PARRATT32 simulations.[39] The layer thickness and roughness values of the high- and low-z mediums were allowed to vary in the fitting process. The density of the high-z medium (W layers) was also allowed to change during the fitting in order to match the measured XRR data, especially in the vicinity of the critical angle of the multilayer. In the fitting process, the optical constants (δ and β) from the Henke's tabulation[34] were used, and deposited thickness values were used as the initial guess. The PARRATT32 fitting yields the following estimates for the microstructural parameters of the multilayer (W/B_4C-1): thickness of W layers $d_w = 16.8$ Å, thickness of B_4C layers $d_{B4C} = 22.5$ Å, and thus multilayer period $d = d_w + d_{B4C}$ is $\sim$39.3 Å. The roughness values of the W and B_4C layers were found to be $\sigma_w = 4.0$ Å and $\sigma_{B4C} = 3.0$ Å respectively. The roughness of the W layers was found to be slightly higher compared to the B_4C layers. It has been reported in the literature that the growth of a high-z layer on a low-z layer (i.e., high-z-on-low-z interface) usually results in a slightly higher roughness compared to the low-z-on-high-z interface.[40,41] Our results show a similar behavior. This arises owing to the difference in the surface free energy of the high- and low-z layers. The measured densities of the W and B_4C layers determined from the best fit results to the XRR data were found to be close to $\sim$90% of the bulk density.

The measured energy dispersive x-ray fluorescence spectrum of the W/B_4C multilayer structure at the Bragg incidence angle ($\theta_{Bragg} = 0.625^\circ$) is shown in Fig. 8(b). In this figure one can clearly observe W-L fluorescence lines (W-Lα, W-Lβ, and W-Lγ), which originate from the constituent layers of W/B_4C multilayer structure. The Si Kα fluorescence peak originates from the Si substrate. In addition, x rays scattered from the multilayer surface (elastic and Compton peaks) are clearly visible. The fluorescence spectrum was recorded for an acquisition time of 200 s.

Figure 9 gives measured Compton and elastic profiles obtained from the W/B_4C multilayer structure in the vicinity of the first Bragg peak, together with the theoretical fitted profiles. From Figs. 9(a) and 9(b), it can be seen that the two profiles (elastic and Compton profiles) are very well correlated at the low and high angle sides of the Bragg peak. This can be explained by understanding the movement of the XSW field as a function of the incidence angle across the Bragg region. As stated earlier, during the first Bragg reflection, an XSW field of periodicity of the multilayer period ($\Delta = d$) is set up inside the multilayer structure (see Fig. 1). At the low angle side of the Bragg peak, the antinodes of the XSW field remain in the low-z layers. As the incidence angle advances across the Bragg region, these antinodes move towards the high-z layers. At the high angle side of the Bragg peak, the XSW antinodes completely coincide with the position of the high-z layers. Because of this movement of the XSW antinodes, the Compton scattering and the elastic scattering yields show a variation over the Bragg region. As is seen in Fig. 9(a), at

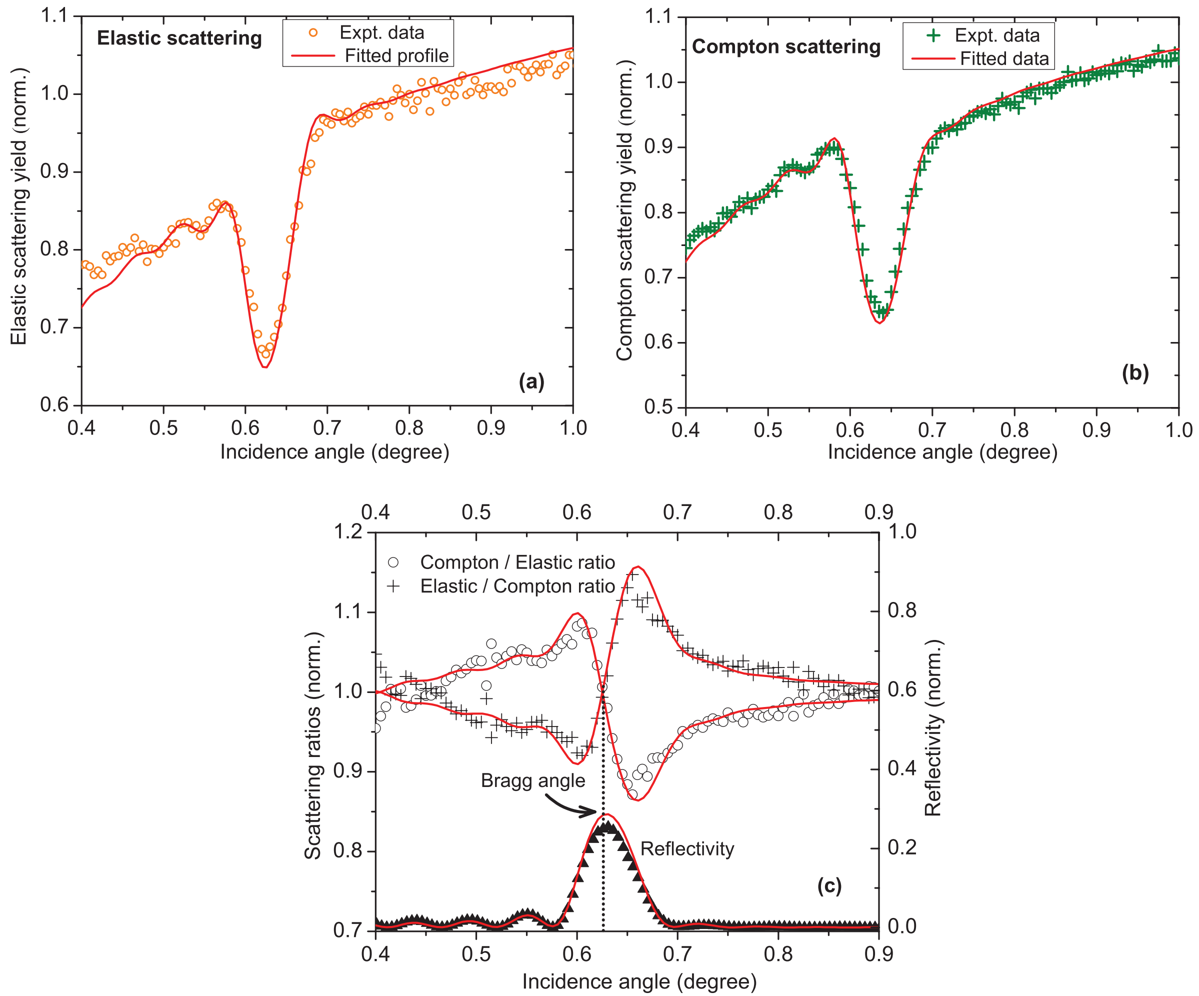

FIG. 9. (Color online) Measured and fitted scattering profiles for the W/B_4C-1 multilayer structure at 15 keV x-ray energy. (a) Elastic scattering, (b) Compton scattering, and (c) scattering ratios. In (c), measured and fitted XRR profiles are also plotted. Scattered points show measured experimental data whereas red solid curves are the best fits to the experimental data.

the high angle side of the Bragg peak, one obtains relatively higher elastic scattering yield compared to the low angle side. This occurs due to the fact that at the higher angle side of the Bragg peak, the XSW antinodes exist in the high-z layers, and therefore one observes an increased elastic scattering yield from the W layers.

On the other hand, the Compton scattering yield varies in a reverse manner, as is evident from Fig. 9(b). At the low angle side of the Bragg peak, one obtains higher Compton scattering intensity compared to the high angle side. This is due to the fact that at the low angle side of the Bragg peak, the XSW antinodes lie in the low-z layers, and therefore one observes an increased elastic scattering contribution from the B_4C layers. The fitted results to the measured elastic and Compton profiles of W/B_4C-1 multilayer gives a value of $d = 39$ Å for the thickness, and $\sigma_w = 4.0$ Å and $\sigma_{B4C} = 2.8$ Å respectively for the roughness values of the W and B_4C layers. Fig. 9(c) presents the Compton and elastic scattering ratios; and the measured and fitted specular reflectivity for the W/B_4C-1 multilayer structure. It can be seen that the angle-dependent scattering ratio profiles, Compton-to-elastic ratio and elastic-to-Compton ratio, intersect each other at a specific point thereby providing a very precise estimate for the Bragg angle, which is $\theta_{Bragg} \sim 0.626 \pm 0.001$. It is also possible to obtain the position of the Bragg angle by differentiating either of the scattering ratio profiles. However, to make clear how the Compton and the elastic scattering intensities can be used to obtain the position of the Bragg angle in a precise way, we have plotted two scattering ratio profiles. On the other hand, it is not easy to get a precise estimate of the Bragg angle from the XRR profile, due to the relatively large flat top in the XRR peak, as is evident from this figure.

The XSW induced fluorescence measurements performed on the W/B_4C-1 multilayer structure are presented in Fig. 10. Here, W-Lα fluorescence intensity has been plotted along with the measured XRR data as a function of incidence angle over the Bragg peak region. For fitting of the fluorescence and reflectivity experimental data, we have used microstructural parameters determined from the best fit results of the XSW induced Compton and elastic scattering measurements. It can be seen from this figure that the fitted profiles show a good agreement with the measured data. The inset of Fig. 10 shows the determined surface roughness of the individual high- and low-z layers. These values are determined by optimizing

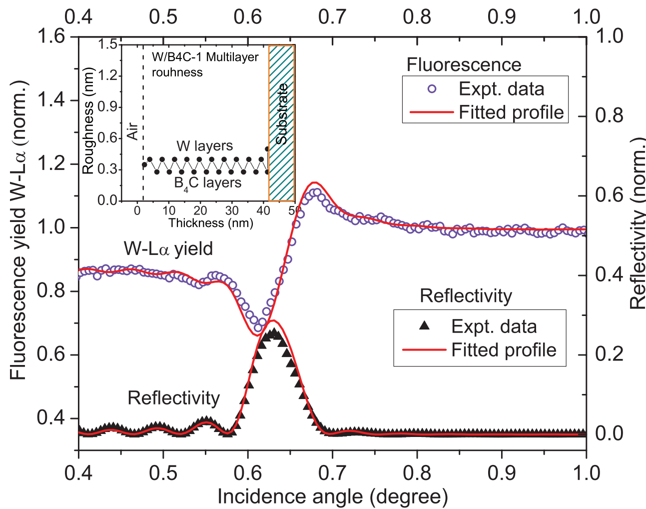

FIG. 10. (Color online) The XSW induced W-Lα fluorescence and XRR profiles observed from the W/B_4C-1 multilayer structure at 15 keV x-ray energy. Scattered points show measured experimental data whereas red solid curves are the best fits to the experimental data. In the inset, determined surface roughness values of individual high- and low-z layers are shown.

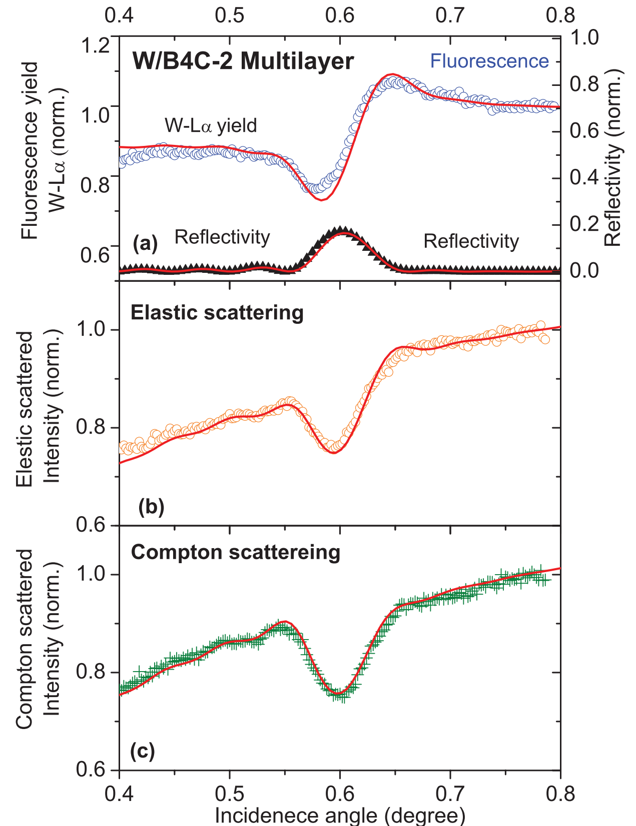

FIG. 11. (Color online) Measured W-Lα fluorescence and scattering profiles for the W/B_4C-2 multilayer structure at 15 keV x-ray energy. (a) W-Lα fluorescence profile. The measured XRR profile is also shown. (b) Elastic scattering, (c) Compton scattering. Scattered points show measured experimental data whereas red solid curves are the best fits to the experimental data.

all the three XSW profiles (Compton, elastic, and W-Lα fluorescence) collectively in a semiempirical fitting loop in which the roughness of individual layers of the multilayer structure is optimized. The fitting yields surface roughness values of the W and B_4C layers to be $\sigma_w = 4.0$ Å and $\sigma_{B4C} = 2.8$ Å respectively. The surface roughness of the top B_4C layers is found to be somewhat higher $(\sigma_{B4C})_{\text{Top layer}} \sim 3.5$ Å. This could be either due to the oxidation of the top layer or due to the presence of an additional layer of very low density and high roughness generated during handling of the sample in the ambient environment.

Finally, the method presented has been applied to another periodic multilayer structure (W/B_4C-2) composed of much interface properties compared to the W/B_4C-1 structure. While the d period (~41 Å) and the bilayer period ($N = 10$) values of the W/B_4C-2 multilayer are maintained close to those of the W/B_4C-1, the surface roughness of the W layers in W/B_4C-2 is modified without much changing the roughness properties of the B_4C layers. This is obtained by adjusting the multilayer deposition conditions like the distance between deposition targets and substrate mounting holder and the sputtering rate for W deposition.

The XSW induced measurements performed on W/B_4C-2 are presented in Fig. 11. Figure 11(a) shows the measured XSW induced W-Lα fluorescence and the x-ray reflectivity profiles, together with the fitted results. By comparing Figs. 10 and 11(a), it can be seen that the Kiessig fringes are not clearly visible in the measured fluorescence profile on the low and high angle sides of the Bragg peak. Similar results are also obtained for the measured elastic [cf. Figs. 9(a) and 11(b)] and Compton [cf. Figs. 9(b) and 11(c)] scattering profiles. This effect occurs if the interface roughness of constituent layers of the periodic multilayer structure increases. As explained in Sec. III A, if the interface roughness of the high- and low-z layers of the periodic multilayer structures increases then it reduces the contrast of the main XSW oscillations in the vicinity of the Bragg peak as well as for the nearby Kiessig fringes in the measured angle dependent fluorescence, elastic, and Compton scattering profiles. Our experimental results presented in Figs. 11(a)–11(c), clearly demonstrates this effect. The best fits results of all the three profiles (W-Lα fluorescence, elastic, and Compton) provided microstructural parameters of the W/B_4C-2 multilayer structure; thickness of W layers $d_w = 16.6$ Å, thickness of B_4C layers $d_{B4C} = 24.5$ Å, and thus multilayer period $d \sim 41.1$ Å. The roughness values of the W and B_4C layers are found to be $\sigma_w = 8.8$ Å and $\sigma_{B4C} = 4.3$ Å respectively.

It has been shown that the Compton and elastic scattering profiles can be consistently used to derive microstructural parameters of the periodic multilayer structures such as thickness of layers, surface roughness, and the interface diffusion between the high- and low-z layers. Combining these results with those obtained from the fluorescence and specular x-ray reflectivity measurements can give even a greater confidence in the derived parameters. It is therefore suggested to utilize the combined XSW analysis approach using the fluorescence, elastic, and Compton scattering profiles with the XRR data in a self-consistent manner, to achieve greater accuracies in the determination of microstructural parameters of the

periodic multilayer structures. Furthermore, in contrast to the conventional XSW fluorescence approach where the analysis of the low-z element is a challenge, the methodology described here provides an opportunity to analyze both the high- and low-z layers independently.

VI. CONCLUSION

We have demonstrated an approach to evaluate microstructural parameters of the periodic multilayer structures using the XSW enhanced elastic and Compton scattering measurements. Our results indicate that the scattered x rays (elastic and Compton) emitted from nanometer scaled thin multilayer structures can be used as a sensitive probe to establish structural parameters of both the high- and low-z layers independently. The method has been validated by analyzing two different repetitive W/B_4C multilayers composed of different surface and interface properties. It may be mentioned that the present approach greatly overcomes the limitation of the fluorescence assisted XSW method and therefore it is especially suitable for characterizing thin layered materials consisting of the low-z medium including soft matter such as Langmuir-Blodgett films, polymer films, and biological enzyme sensor films. We believe that the proposed technique will lead to further experimental studies in a wide range of interesting applications related to nanoscaled thin film medium and analysis of the defects and empty spaces in crystals using the Compton enhanced x-ray standing wave investigations.

ACKNOWLEDGMENTS

This work was carried out with the support of Diamond Light Source Ltd. UK. We thank A. Malandain for technical assistance during the experiment setup on B16 Test beamline at Diamond. P. N. Rao is acknowledged for providing help in fabricating thin periodic W/B_4C multilayer structures.

APPENDIX

The photon-matter interaction in the x-ray energy range of 0.1-1000 keV is mainly described by three processes. These are Rayleigh (elastic) scattering, Compton (inelastic) scattering and photoionization. The scattering of x rays from a single electron can be described by the Thomson scattering and has a total cross section $\sigma_{\text{Thomson}} = \frac{8\pi r_0^2}{3}$, where r_0 is the classical electron radius ($r_0 = e^2/m_e c^2 \approx 2.812 \times 10^{-15}$ meter). The scattering of x rays from a multielectron system such as atoms involves combined contribution of all the electrons. The total elastic x-ray cross section for an atom is expressed by

$$\sigma_{\text{Elastic}} = \frac{8\pi r_0^2}{3} |f^0(E_0)|^2$$

where $f^0(E_0)$, is the complex atomic scattering factor at particular scattering angle. In the Thomson and elastic scattering processes the incident and scatter photons comprise of same energy. If the incident photon energy E_0, is larger than the tightly bind core electrons of an atom, the complex atomic scattering factor $f^0(E_0)$ reduced to $\approx$-z (atomic number) and the total elastic cross section becomes $\sigma_{\text{Elastic}} \approx \sigma_{\text{Thomson}} \times z^2$. In fact, both the elastic and the Compton scattering processes can be explained from the Thomson scattering by modifying the scattering from a point charge to account for the extended charge distribution of all the electrons of an atom through the use of form factor (i.e. atomic scattering factor) and incoherent scattering factor.[42,43] In a good agreement, the Compton cross section σ_{Compton} per electron is given by Klein-Nishina formula[44]

$$\sigma_{\text{Compton}} \cong \sigma_{KN} = \sigma_{\text{Thomson}} \times \left(\frac{1 + 2\gamma + 1.2\gamma^2}{(1 + 2\gamma)^2} \right)$$

$$\gamma = \left(\frac{E_0}{mc^2} \right)$$

At high photon energies, the total Compton cross section for an atom containing-z electrons becomes $\sigma_{\text{Compton}} \approx z\sigma_{KN}$.

---

*Corresponding author: mktiwari@rrcat.gov.in

[1] E. Spiller, Appl. Phys. Lett. **20**, 365 (1972).
[2] T. W. Barbee, *Synthetic Modulated Structure Materials* (Academic Press, New York, 1985), p. 313.
[3] D. L. Windt, S. Donguy, C. J. Hailey, J. Koglin, V. Honkimaki, E. Ziegler, F. E. Christensen, H. Chen, F. A. Harrison, and W. W. Craig, Appl. Opt. **42**, 2415 (2003).
[4] K. Wellock, S. J. C. H. Theeuwen, J. Caro, N. N. Gribov, R. P. van Gorkom, S. Radelaar, F. D. Tichelaar, B. J. Hickey, and C. H. Marrows, Phys. Rev. B **60**, 10291 (1999); A. T. Costa, Jr., A. C. de Castro Barbosa, J. d Albuquerque e Castro, and R. B. Muniz, J. Phys.: Condens. Matter **13**, 1827 (2001).
[5] J. H. Kim, I. Vrejoiu, Y. Khaydukov, T. Keller, J. Stahn, A. Rühm, D. K. Satapathy, V. Hinkov, and B. Keimer, Phys. Rev. B **86**, 180402(R) (2012).
[6] P. Zahn, N. Papanikolaou, F. Erler, and I. Mertig, Phys. Rev. B **65**, 134432 (2002).
[7] B. Revaz, M. C. Cyrille, B. L. Zink, I. K. Schuller, and F. Hellman, Phys. Rev. B **65**, 094417 (2002).
[8] L. G. Parratt, Phys. Rev. **95**, 359 (1954).
[9] S. K. Sinha, E. B. Sirota, S. Garoff, and H. B. Stanley, Phys. Rev. B **38**, 2297 (1988).
[10] D. Dale, A. Fleet, Y. Suzuki, and J. D. Brock, Phys. Rev. B **74**, 085419 (2006); Z. Jiang, D. R. Lee, S. Narayanan, J. Wang, and S. K. Sinha, *ibid.* **84**, 075440 (2011).
[11] D. K. G. de Boer, Phys. Rev. B **44**, 498 (1991).
[12] S. K. Ghose and B. N. Dev, Phys. Rev. B **63**, 245409 (2001).
[13] A. Krol, C. J. Sher, and Y. H. Kao, Phys. Rev. B **38**, 8579 (1988).
[14] M. Kramer, A. von Bohlen, C. Sternemann, M. Paulus, and R. Hergenrodera, J. Anal. At. Spectrom. **21**, 1136 (2006).
[15] M. Drakopoulos, J. Zegenhagen, T. L. Lee, A. Snigirev, I. Snigireva, V. Cimalla, and O. Ambacher, J. Phys. D: Appl. Phys. **36**, A214 (2003).
[16] M. K. Tiwari, S. R. Naik, G. S. Lodha, and R. V. Nandedkar, Anal. Sci. **21**, 757 (2005).
[17] B. W. Batterman, Phys. Rev. **133**, A759 (1964).
[18] J. A. Golovochenko, B. W. Batterman, and W. L. Brown, Phys. Rev. B **10**, 4239 (1974).

[19]M. J. Bedzyk, G. Materlik, and M. V. Kovalchuk, Phys. Rev. B **30**, 2453 (1984).
[20]M. J. Bedzyk, G. M. Bommarito, and J. S. Schildkraut, Phys. Rev. Lett. **62**, 1376 (1989).
[21]M. J. Bedzyk, D. H. Bilderback, G. M. Bommarito, M. Caffrey, and J. S. Schildkraut, Science **241**, 1788 (1988).
[22]H. Schwenke and J. Knoth, *Handbook of X-Ray Spectrometry*, edited by R. E. Van Grieken, and A. A. Markowicz (Marcel Dekker, New York, 1993), p. 453.
[23]D. P. Woodruff, Rep. Prog. Phys. **68**, 743 (2005), and references therein; U. Weisbrod, R. Gutschke, J. Knoth, and H. Schwenke, Fresenius' J. Anal. Chem. **341**, 83 (1991).
[24]M. K. Tiwari, G. M. Bhalerao, M. Babu, A. K. Sinha, and C. Mukherjee, J. Appl. Phys. **103**, 054311 (2008).
[25]M. K. Tiwari, K. J. S. Sawhney, Tien-Lin Lee, S. G. Alcock, and G. S. Lodha, Phys. Rev. B **80**, 035434 (2009).
[26]T. Kawamura, and H. Takenaka, J. Appl. Phys. **75**, 3806 (1994); V. Kohli, M. J. Bedzyk, and P. Fenter, Phys. Rev. B **81**, 054112 (2010).
[27]T. Matsushita, A. Iida, T. Ishikawa, T. Nakagiri, and K. Sakai, Nucl. Instrum. Methods Phys. Res., Sect. A **246**, 751 (1986).
[28]T. Salditt, T. H. Metzger, J. Peisl, and R. Feidenhans, J. Appl. Phys. **83**, 5179 (1998).
[29]J. B. Kortright, and A. Fischer-Colbrie, J. Appl. Phys. **61**, 1130 (1987).
[30]W. H. McMaster, N. K. Del Grande, J. H. Mallett, and J. H. Hubbell, Report No. UCRL-50174, Section II, Revision-I, (1969), http://cars9.uchicago.edu/mcbook/.
[31]J. H. Hubbell, W. H. McMaster, N. K. Del Grande, and J. H. Mallett, *International Tables for X-ray Crystallography*, Vol. 4, edited by J. A. Ibers and W. C. Hamilton (Kynoch Press, Birmingham, 1974), pp. 47–70.
[32]M. Sánchez del Río and R. J. Dejus, Proc. SPIE **3152**, 148 (1997).
[33]http://csrri.iit.edu/periodic-table.html.
[34]http://henke.lbl.gov/optical_constants/pert_form.html
[35]M. K. Tiwari and K. J. S. Sawhney, J. Phys.: Condens. Matter **22**, 175003 (2010).
[36]K. D. Shaw and A. S. Krieger, Appl. Opt. **28**, 1052 (1989).
[37]G. S. Lodha, RRCAT News Lett. **22**, 7 (2009).
[38]K. J. S. Sawhney, I. P. Dolbnya, M. K. Tiwari, L. Alianelli, S. M. Scott, G. M. Preece, U. K. Pedersen, and R. D. Walton, AIP Conf. Proc. **1234**, 387 (2010).
[39]C. Braun, HMI Berlin, Germany, PARRATT32: The reflectivity Tool, Ver. 1.6, (1998).
[40]Amanda K. Pettford-Long, M. B. Stearns, C. H. Chang, S. R. Nutt, D. G. Stearns, N. M. Ceglio, and A. M. Hawryluk, J. Appl. Phys. **61**, 1422 (1987).
[41]D. E. Savage, N. Schimke, Y. H. Phang, and M. G. Lagally, J. Appl. Phys. **71**, 3283 (1992).
[42]R. Ribberfors and K. F. Berggren, Phys. Rev. A **26**, 3325 (1982).
[43]J. H. Hubbell, W. J. Veigele, E. A. Briggs, R. T. Brown, D. T. Cromer, and R. J. Howerton, J. Phys. Chem. Ref. Data **4**, 471 (1975).
[44]O. Klein and Y. Nishina, Z. Physik **52**, 853 (1929) (in German).